Electronic Supplementary Information

iR Drop in Scanning Electrochemical Cell Microscopy

Brandon Blount, Gabriel Juarez, Yufei Wang, and Hang Ren*

Department of Chemistry, The University of Texas at Austin, 105 E 24th St, Austin, TX 78712.

Table of Contents

1. Experimental Methods

Chemicals and Materials

Ferrocene (Aldrich, 98%), perchloric acid (Fisher, 70%), ruthenium hexafluoride trichloride $Ru(NH_3)_6Cl_3$ (Sigma Aldrich, 98%), potassium chloride (Fisher, 99%), potassium nitrate (Fisher, 98%), propylene carbonate anhydrous (Sigma Aldrich, 99.7%) were used as received. All aqueous solutions were prepared using ultra-pure water (Thermo Scientific GenPure, 18.2 MΩ cm). Tetrabutylammonium hexafluorophosphate (Fisher, 98%) was purified by recrystallization in ethanol three times and dried under vacuum for 72 hrs. Pt foil (Alfa Aesar, 99.9%). was flame annealed in H_2 (99.999%, Praxair). Ag/AgCl quasi-reference counter electrodes were prepared by exposing the freshly polished Ag wires (99.99%, 0.125 mm o.d.) in a bleach solution for 30 min, which is rinsed with ultra-pure water.

Fabrication of Nanopipettes Single and Dual Barrel

Single-barrel and dual-barrel pipettes were pulled from quartz capillaries (single barrel: 1.0 mm i.d., 0.7 mm o.d; dual barrel: 1.2 mm i.d., 0.9 mm o.d, Sutter). The size of the nanopipette was characterized by scanning electron microscopy (Thermo Fisher Scios 2 DualBeam, FEI Quanta 650FEG).

SECCM Setup

SECCM experiments were performed using a homebuilt scanning electrochemical probe setup using the Warwick Electrochemical-Scanning Probe Microscopy Platform (WEC-SPM) software, which was generously provided by Professor Pat Unwin. based on Prof. Unwin's design.[1] The pipette was moved using an x-y piezo (NPXY300-291, nPoint) and a z piezo (P-621.1CD, PI). The scanning probe apparatus and preamplifiers were concealed in a custom-built Faraday cage on a vibration isolation table (Vision IsoStation, Newport). The current was recorded using Axopatch 200 B (Axon) with CV 203BU headstage or a Dagan preamplifier unit (CHEM-HS, Dagan Corporation). All the potentials reported in this paper are referenced to the Ag/AgCl wire electrode. The data acquisition and instrument control were interfaced through the analog input and output channels using an FPGA card (PCIe-7846, National Instruments).

2. Pipette Characterization

The diameters of the pipette opening are measured by SEM as shown in Figure S1, which yield 220 nm and 150 nm for single- and dual-barrel pipettes, respectively. The half-cone angle is measured to be 10° and 20° for single-barrel and dual-barrel pipettes, respectively.

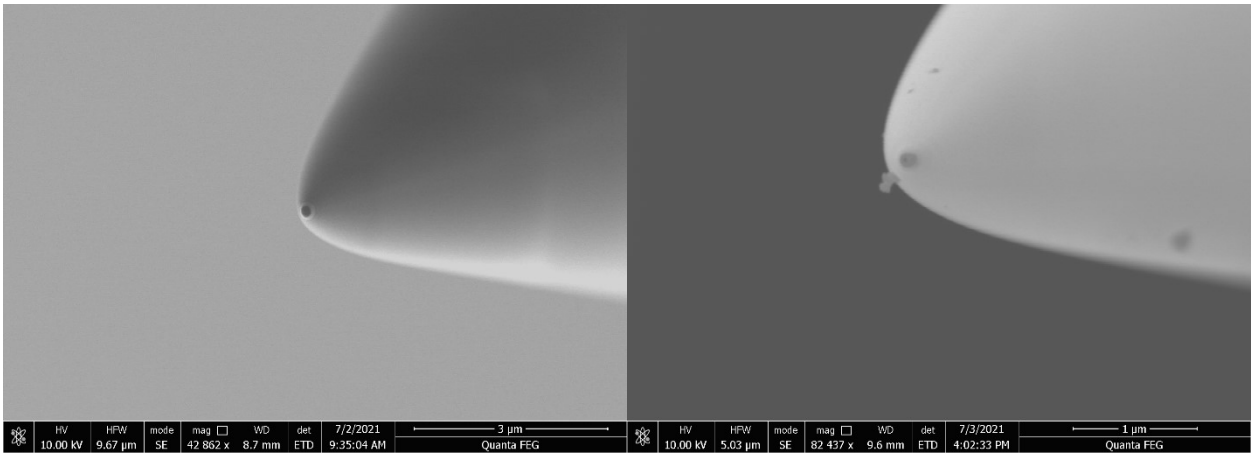

Figure S1. SEM images of a single-barrel pipette (left) and a dual-barrel pipette (right).

3. Derivation of Solution Resistance (R_s) in Single-Barrel SECCM

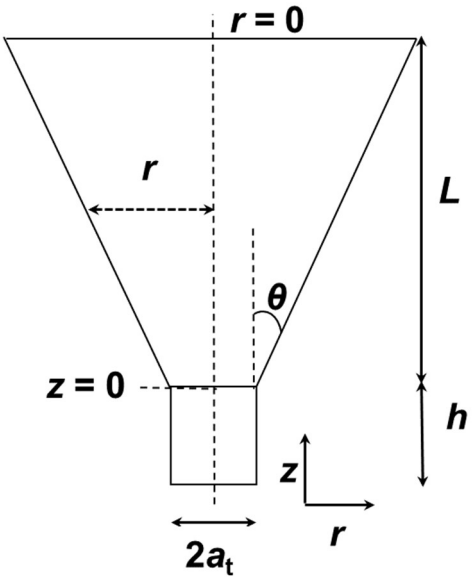

Figure S2. The geometry of a single-barrel pipette for deviation of solution resistance.

Assuming a cylindrical droplet with a radius equivalent to that of the pipette tip, a_t, and a height h, as shown in Figure S2, the resistance in the droplet, R_d, is derived as:

$$R_{\mathrm{d}} = \int_{-h}^{0} \frac{\mathrm{d}z}{\kappa A} = \frac{h}{\kappa \pi a_t^2} \tag{S1}$$

For the conical region, the disk segment area (πr^2) varies along the axial direction of the cone. The solution resistance within this pipette region (R_{p}) can be derived by integration along the axial of the pipette (z):

$$R_{\mathrm{p}} = \int_{0}^{L} \frac{dz}{\kappa \pi r^2} \tag{S2}$$

Using trigonometry, it can be shown that:

$$r = z\tan(\theta) + a_t \tag{S3}$$

Substituting eq S3 to S2 yields:

$$R_{\mathrm{p}} = \frac{1}{\kappa \pi \tan(\theta)} \int_{0}^{L} \frac{d(z\tan(\theta) + a_t)}{(z\tan(\theta) + a_t)^2} = -\frac{1}{\kappa \pi \tan(\theta)} \left[\frac{1}{z\tan(\theta) + a_t}\right]_0^L \tag{S4}$$

Further simplification results in:

$$R_{\mathrm{p}} = \frac{L}{\kappa\pi a_t(a_t + L\tan(\theta))} \tag{S5}$$

The summation of equation S1 and equation S4 gives the total solution resistance (R_{s}):

$$R_{\mathrm{s}} = R_{\mathrm{d}} + R_{\mathrm{p}} = \frac{h}{\kappa\pi a_t^2} + \frac{L}{\kappa\pi a_t(a_t + L\tan(\theta))} \tag{S6}$$

4. Additional Results from Single-Barrel SECCM Experiments

As described in the main text for Fc oxidation, another single-barrel SECCM experiment was performed for the proton reduction in 100 mM $HClO_4$, with 0 mM and 100 mM KNO_3. Using eq 2 from the main text, *iR* drop was corrected for as shown in Figure S3. As expected, a small *iR* correction (up to 40 mV) is observed in the voltammograms for the solution containing 0 mM KNO_3 (Figure S3a), while a much smaller *iR* drop (< 15 mV) is observed in the voltammograms for the solution containing 100 mM KNO_3 solution.

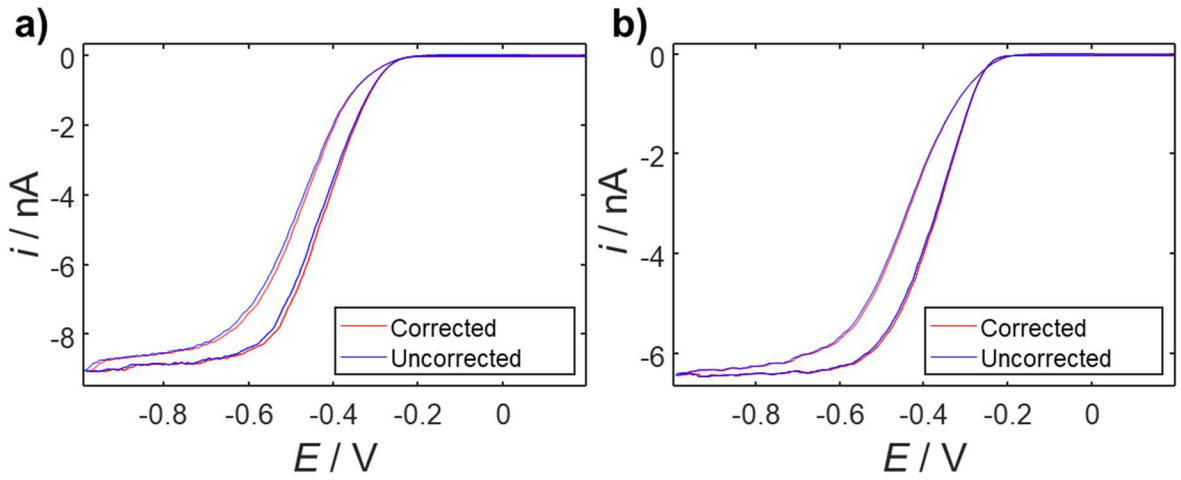

Figure S3. Uncorrected (blue) and *iR* drop corrected (red) single-barrel SECCM voltammograms. Solution contains 100 mM $HClO_4$, 1 mM KCl, and a) 1 mM KNO_3 b) 100 mM KNO_3. *iR* drop is corrected using a calculated R_s from eq 2 (or eq S6).

5. Finite Element Simulation

The finite element simulation of single- and dual-barrel SECCM experiments were performed by solving the steady-state Nernst-Planck equation with electroneutrality using COMSOL Multiphysics:

$$J_i = -z_\mathrm{i} u_\mathrm{i} F c_\mathrm{i} \nabla \phi \; - \; D_\mathrm{i} c_\mathrm{i} \tag{S7}$$

$$\sum_\mathrm{i} z_\mathrm{i} c_\mathrm{i} = 0 \tag{S8}$$

And the current can be expressed as

$$i = F \sum_\mathrm{i} z_\mathrm{i} J_\mathrm{i} \tag{S9}$$

a. Simulation of Single-Barrel SECCM Experiment

For the simulation of single-barrel SECCM, a 2D-axial symmetry was used for better computational efficiency. The geometry of the pipette with boundaries labeled is shown in Figure S4. The geometry of the single-barrel pipette used for simulation has a length of 100 μm, a half-cone angle of 10°, and a tip radius of 315 nm. Without losing generality, the substrate-droplet contact angle was 90° with a droplet of height equal to the pipette tip radius. The boundary conditions are summarized in Table S1. Butler-Volmer kinetics is used for the electrode kinetics, and the electrode potential used in the is E_app-E_ir, where E_ir is the *iR* drop obtained in the simulation.

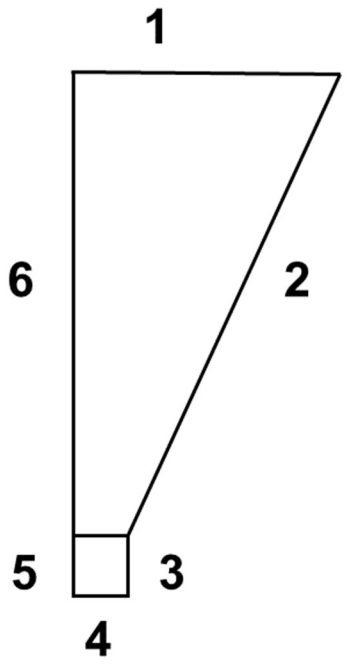

Figure S4. The geometry of the model for single-barrel SECCM with boundaries labeled (not drawn to scale).

Table S1: Boundary conditions and corresponding boundaries for single-barrel SECCM

Boundary conditions	Comment	Boundary numbers
$\boldsymbol{n} \cdot \boldsymbol{J}_{\mathbf{i}} = 0$	No flux	2, 3
$c_i = c_{0,i}$	Constant concentration	1
$\boldsymbol{n} \cdot \boldsymbol{J}_{\mathbf{i}} = J_{0,\mathrm{i}}$ $\boldsymbol{n} \cdot \boldsymbol{i} = i_0$	Faradaic reactions using Butler-Volmer kinetics Electrical current	4
$V = 0$	Ground	1
$\boldsymbol{n} \cdot \boldsymbol{i} = 0$	Electric Insulation	2, 3
	Axial Symmetry	5, 6

In addition to the Fc system as shown in the main text, the raw *iR*-uncorrected and the *iR*-free voltammograms are simulated in proton reduction and $\mathrm{Ru(NH_3)_6^{3+}}$ reduction system as shown in Figure S5 and S6, respectively. Eq 2 and eq 7 are applied to the uncorrected raw voltammograms (black curves) to compensate for the *iR* drop, and the corrected voltammogram (star and dot in Figures S5 and S6) is then compared with the ideal *iR*-free one (blue curves in Figures S5 and S6).

As shown in both the proton reduction and $\mathrm{Ru(NH_3)_6^{3+}}$ reduction systems, equations 2 and 7 both estimate a constant R_s that are on the same order of magnitude when compared with the simulation. Again, a change in R_s is observed in the simulation at different potential. In the proton reduction system, the *iR* drop is large as the current for proton reduction is high (Figure S5). However, in the $\mathrm{Ru(NH_3)_6^{3+}}$ reduction system as shown in Figure S6, the the voltammetric current is relatively small, and therefore *iR* drop is negligible.

We also notice a larger discrepancy of the calculated R_s between eq 2 and eq 7 for the $\mathrm{Ru(NH_3)_6^{3+}}$ reduction and proton reduction system (Figure S5b and Figure S6b), while a very small discrepancy is observed in the Fc system (Figure 3b). This is likely due to the contribution of migration current to the i_{lim}, which are used in eq 7. Note that the derivation of eq 7 is based on diffusion as the only mode of mass transport. As described in the main text, the analytical solutions also assume a constant solution conductivity, κ, which is shown to vary with applied potential and distance from the electrode surface in Figures S5c-d and S6c-d. This also explains the difference in *iR* correction of the analytical solution and the simulated *iR*-free.

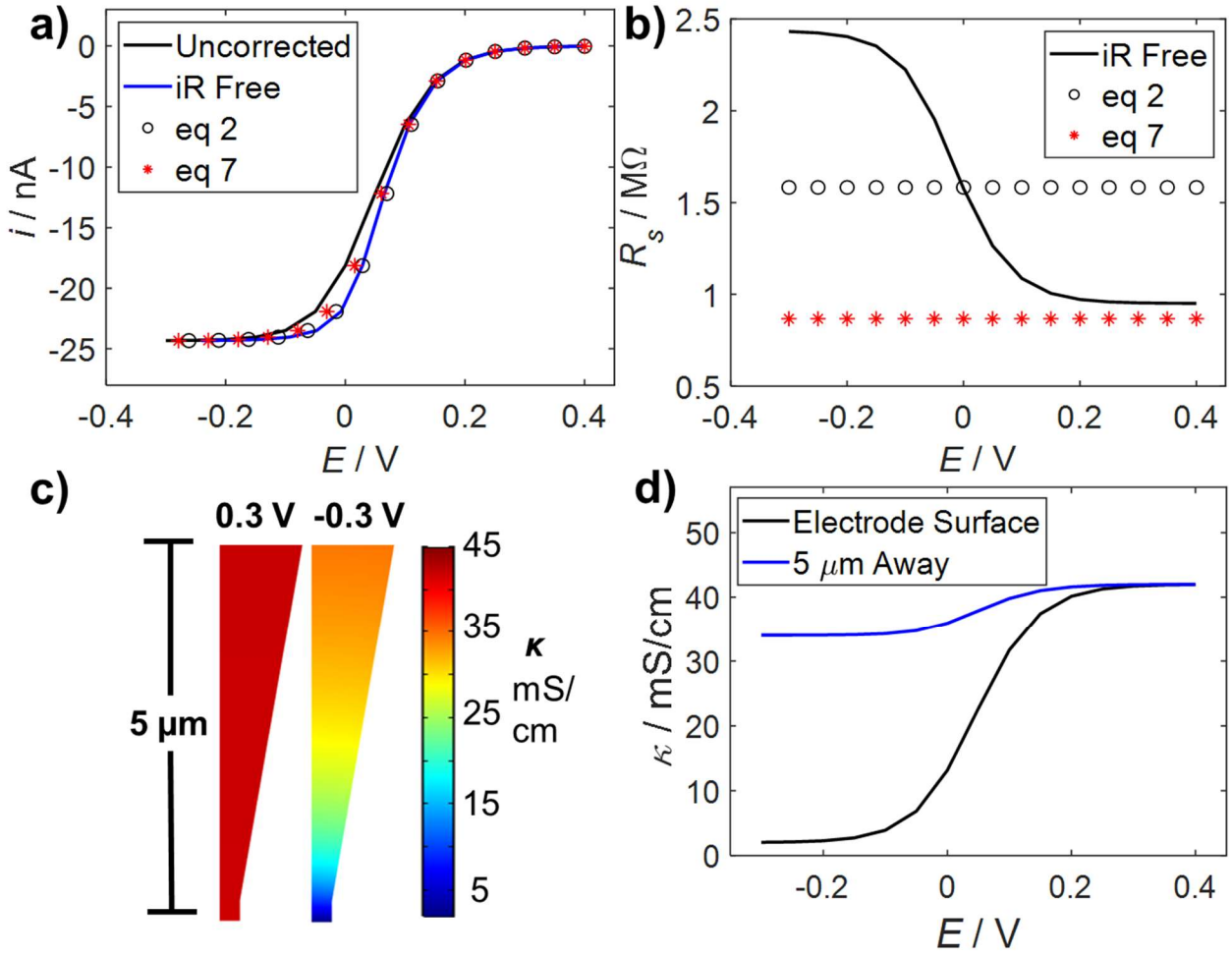

Figure S5. a) Simulation of proton reduction in 100 mM $HClO_4$ and 1 mM KNO_3 showing a) the steady-state voltammograms with no correction (black), ideal *iR*-free (blue), and correction by eq 2 (black circle) and eq 7 (red star). b) Solution resistance during the voltammetry. c) Solution conductivity profiles at the electrode surface up to a distance of 5 µm along the pipette. d) Solution conductivity plots as a function of the applied potential at the electrode surface and at 5 µm along the axisymmetric line.

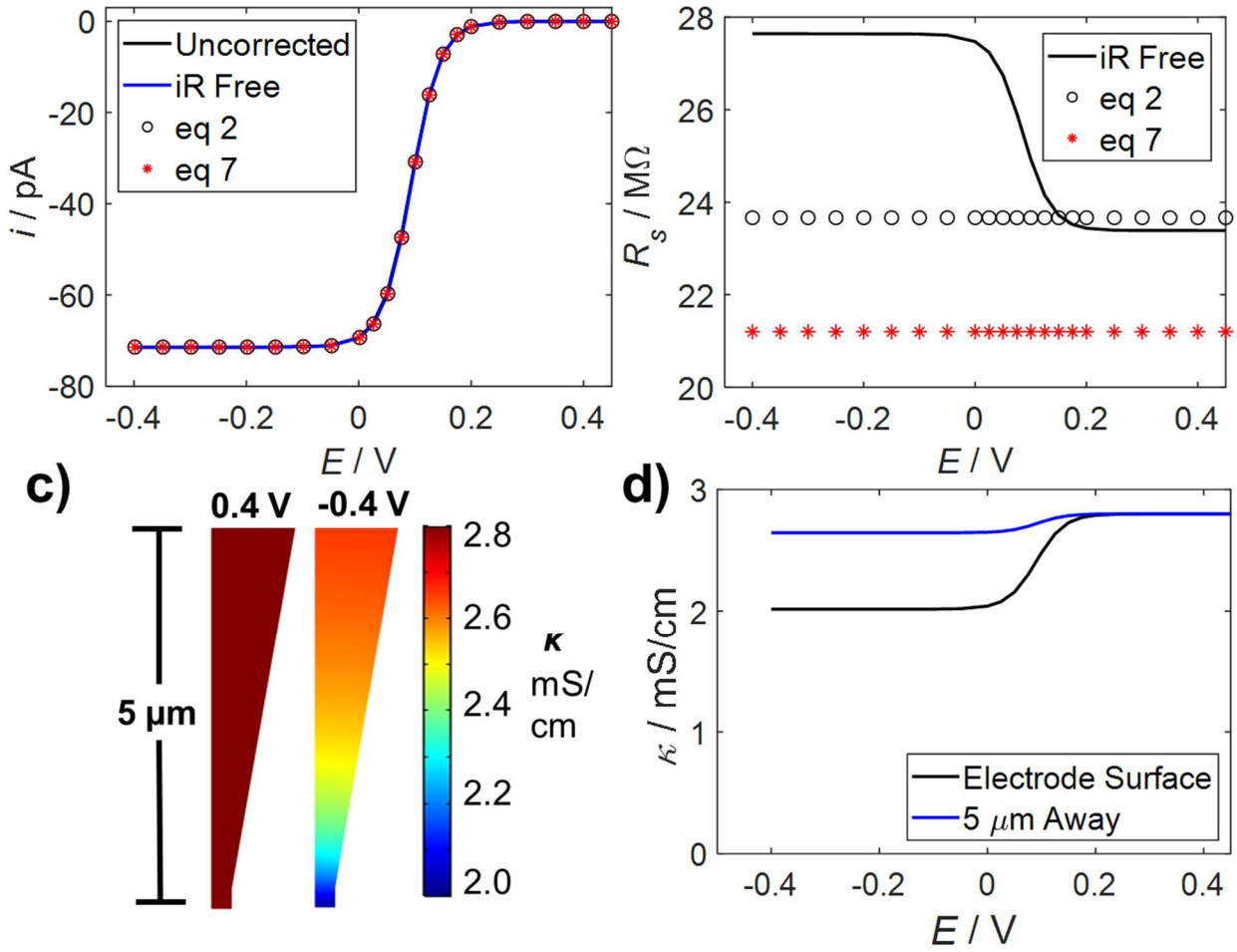

Figure S6. Simulation of the reduction of $\mathrm{Ru(NH_3)_6^{3+}}$ in 1 mM KNO_3 showing a) the steady-state voltammograms with no correction (black), ideal *iR*-free (blue), and correction by eq 2 (black circle) and eq 7 (red star). b) Solution resistance during the voltammetry. c) Solution conductivity profiles at the electrode surface up to a distance of 5 μm along the pipette. d) Solution conductivity plots as a function of the applied potential at the electrode surface and at 5 μm along the axisymmetric line.

b. Simulation of Dual-Barrel SECCM Experiment

A 3D model is used for the dual-barrel SECCM simulation. A symmetry boundary (the cut plane to reveal the half of the dual-barrel pipette as shown in Figure S7) was utilized to reduce computation time. The geometry of the simulation was defined by the pipette length, half-cone angle, tip radius, and substrate-droplet contact angle, which are 100 µm, 20°, 130 nm, and 90°. respectively. The boundary conditions in the simulation are given in Table S2, and the boundaries are labeled in cross-sectional geometry in Figure S7b.

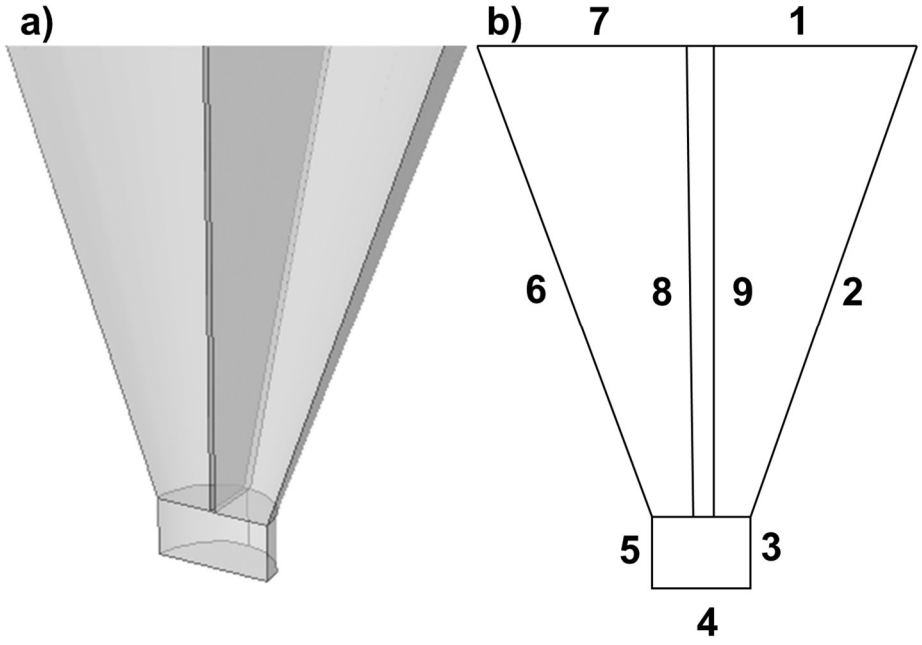

Figure S7. a) 3D geometry of dual-barrel pipette generated using COMSOL Multiphysics with transparent inner-faces and b) cross-sectional schematic with labeled boundaries.

Table S2: Boundary conditions and corresponding boundaries for dual-barrel SECCM

Boundary conditions	Comment	Boundary numbers
$\boldsymbol{n} \cdot \boldsymbol{J}_{\mathbf{i}} = 0$	No flux	2, 3, 5, 6, 8, 9
$c_i = c_{0,i}$	Constant concentration	1, 7
$\boldsymbol{n} \cdot \boldsymbol{J}_{\mathbf{i}} = J_{0,\mathrm{i}}$ $\boldsymbol{n} \cdot \boldsymbol{i} = i_0$	Faradaic reactions using Butler-Volmer kinetics Electrical current	4
$V = 0$	Ground	1
$V = V_2$	Bias potential	7
$\boldsymbol{n} \cdot \boldsymbol{i} = 0$	Electric insulation	2, 3, 5, 6, 8, 9
$\boldsymbol{n} \cdot \boldsymbol{J}_{\mathbf{i}} = 0$	Symmetry	The cross-section plane in Figure S7b.

In addition to the potential bias of 50 mV as described in Figure 6 in the main text, we also show the same reaction with a 100 mV bias is simulated for $\mathrm{Ru(NH_3)_6^{3+}}$ and 20 mM Fc and 1 mM $TBAPF_6$ in propylene carbonate in Figure S8.

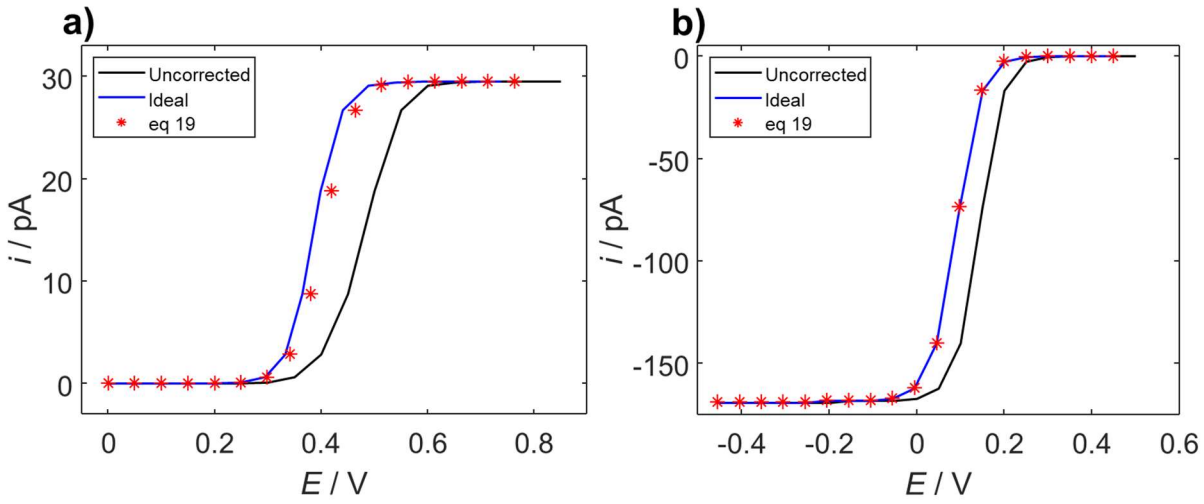

Figure S8. Simulated steady-state uncorrected (black) and ideal *iR*-free (blue) voltammograms of a) 20 mM Fc and 1 mM $TBAPF_6$ and b) 20 mM $\mathrm{Ru(NH_3)_6^{3+}}$ and 1 mM KNO_3. The potential bias (V_2) is 0.1 V.

We also show the potential and concentration profile for the oxidation of Fc to Fc^+ in the finite element simulation. As can be seen from Figures S9-S12, in comparison with Figure 7 of the main text, Fc is oxidized at the contact surface between the substrate and droplet. The bias potential has no effect on the mass transport of Fc owing to its zero charge, while Fc^+ was observed to move toward the more negative potential owing to its positive charge. As shown in Figures S9 and S10, the change in polarity of the bias change the asymmetric distribution of Fc in the barrels. Additional simulated potential profiles and concentration profiles during the voltammetry are shown as Figures S9-S12.

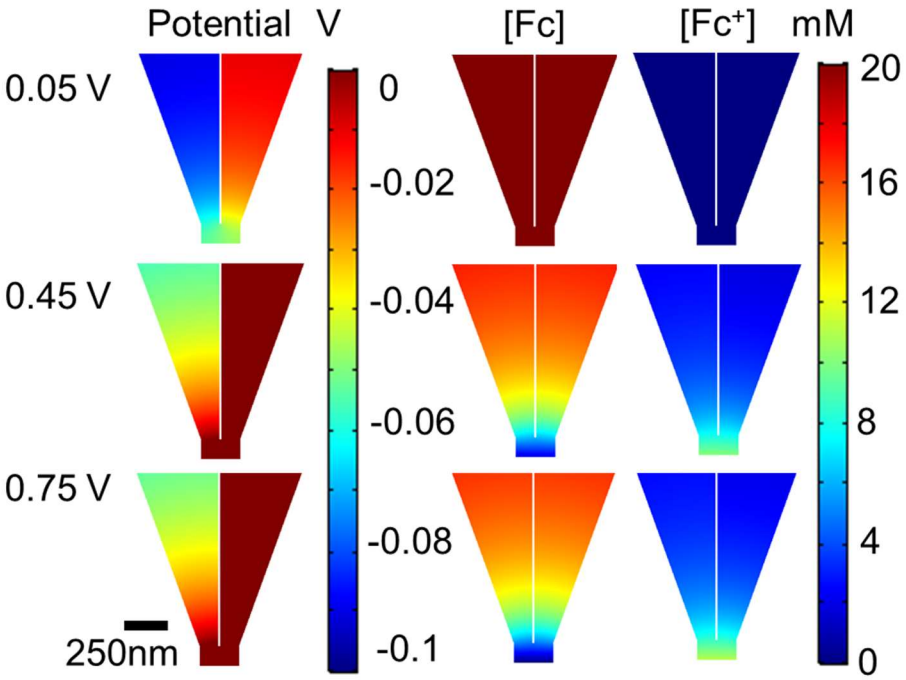

Figure S9. Simulated potential profile and concentration profiles for Fc and Fc^+ with 1 mM $TBAPF_6$ supporting electrolyte at varied substrate potentials. A bias potential (V_2) of -0.1 V is applied.

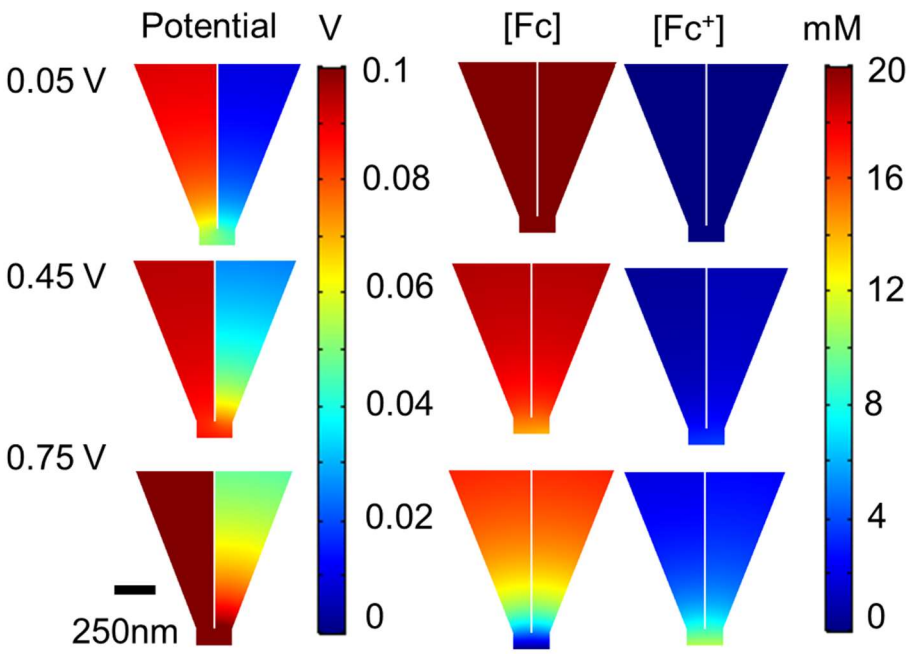

Figure S10. Simulated potential profile and concentration profiles for Fc and Fc^+ with 1 mM $TBAPF_6$ supporting electrolyte at varied substrate potentials. A bias potential (V_2) of +0.1 V is applied.

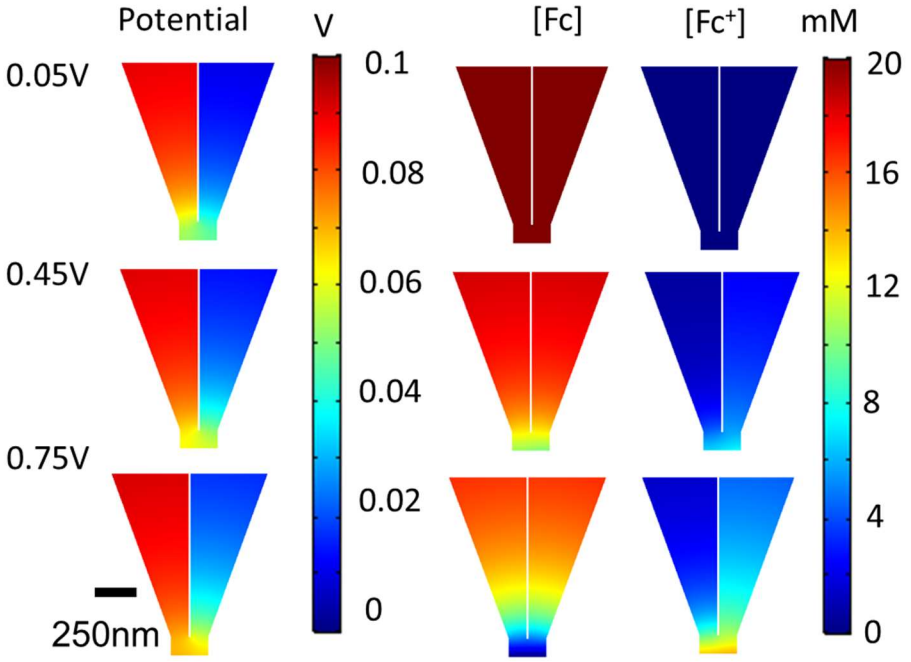

Figure S11. Simulated potential profile and concentration profiles for Fc and Fc^+ with 5 mM $TBAPF_6$ supporting electrolyte at varied substrate potentials. A bias potential (V_2) of +0.1 V is applied.

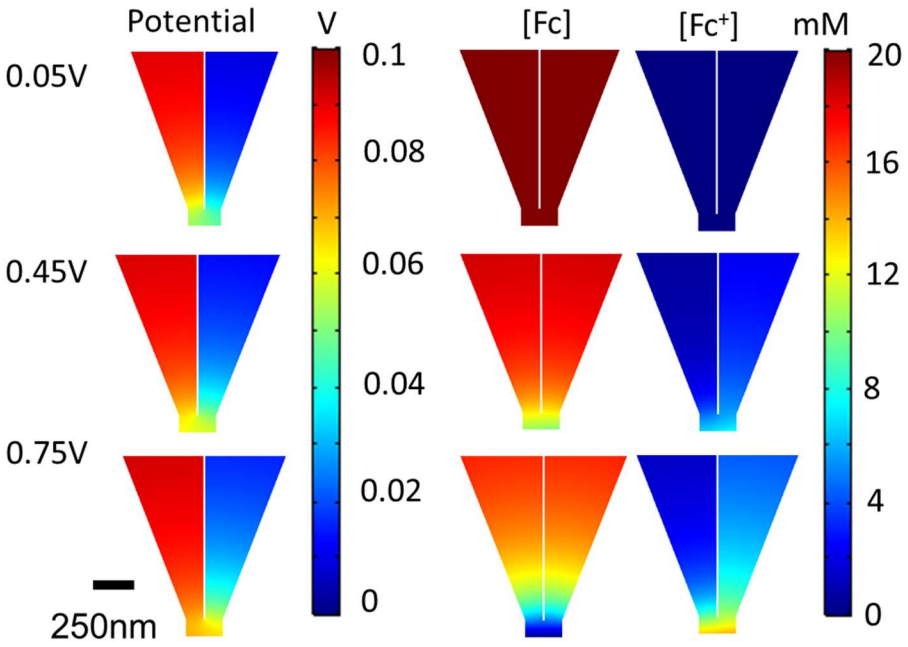

Figure S12. Simulated potential profile and concentration profiles for Fc and Fc^+ with 10 mM $TBAPF_6$ supporting electrolyte at varied substrate potentials. An applied bias potential of 0.1 V is held constant while the substrate potential is changed to 0.05 V, 0.45 V, and 0.75 V.

6. Measuring Solution Resistance in Dual-Barrel SECCM

In the main text Figure 7c, the solution resistance (R_s) obtained using eq 19 behaves as expected: 1) R_s decreases as the concentration of supporting electrolyte increases; 2) R_s decreases as the ionic species, Fc^+, is generated from the neutral Fc at the electrode surface in Faradaic reactions.

Here, we show two other examples of measuring R_s during the voltammetry in dual-barrel SECCM. In the reduction of $\mathrm{Ru(NH_3)_6^{3+}}$, the net result is the replacement of a +3 charged species with a +2 charged one. Therefore, a decrease in the solution conductivity near the electrode surface, or an increase in R_s is expected. A plot of i_1 (Faradaic current) and i_2 vs applied potential is shown in Figure S13. Using eq 19, R_s can be calculated from i_1 and i_2, which is shown in Figure S13c. Indeed, an increase in R_s is observed during the reduction of $\mathrm{Ru(NH_3)_6^{3+}}$. Similarly, for proton reduction reaction, the solution resistance is also expected to increase, which is indeed observed in the measurement as shown in Figure S14.

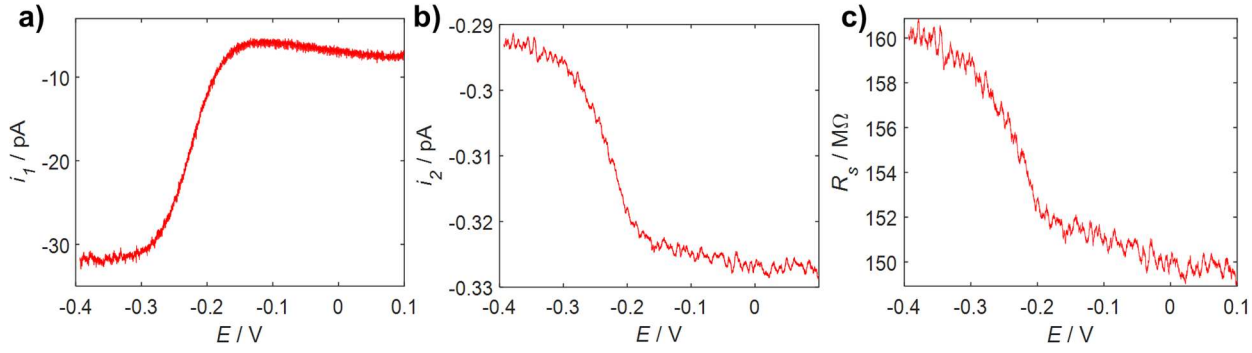

Figure S13. Dual-barrel SECCM voltammograms and corresponding resistance plot with 20 mM $\mathrm{Ru(NH_3)_6^{3+}}$. a) substrate current (i_1). b) current between the barrels (i_2). c) Solution resistance calculated using eq 19. The substrate is Pt with bias potential V_2 = -0.1 V.

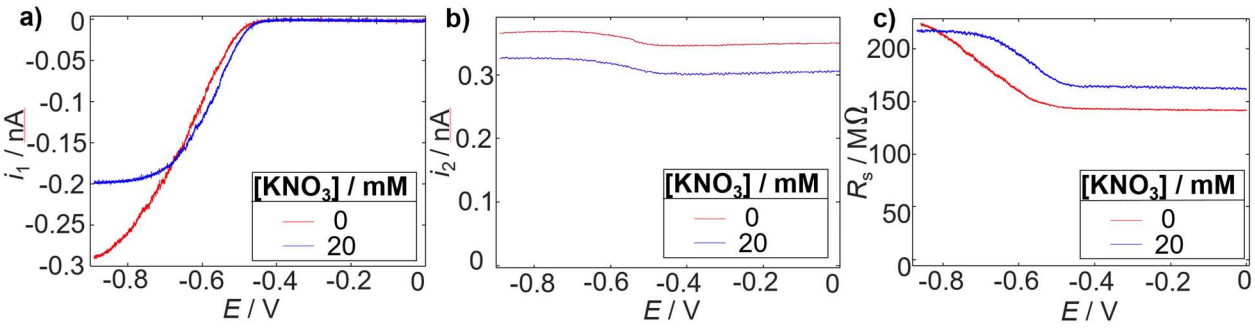

Figure S14. Dual-barrel SECCM voltammograms and corresponding resistance plot with 20 mM $HClO_4$ and 1 mM KCl. a) substrate current (i_1). b) current between the barrels (i_2). c) solution resistance (R_s) calculated using eq 19. The substrate is Pt with bias potential V_2 = 0.1 V.

7. Effect of Noise on *iR* Compensation in Dual-Barrel SECCM

Accurate measurement of i_1 and i_2 is important for *iR* compensation in dual-barrel SECCM using eq 19. This is especially true when the magnitude of the signal is close to the noise level in the measurement (e.g., low pA for the amplifier we use). Note eq 20 involves (i_1 + 2i_2) in the denominator, suggesting the noise in the measurement of i_1 and i_2 can cause the denominator to reach 0, causing a large fluctuation in the corrected potential. To illustrate, a plot of i_2 vs applied potential is shown in Figure S15a, where the magnitude of i_2 itself is close to the noise of the measurement. Directly applying eq 19 for *iR* compensation will result in a corrected with large fluctuation in the potential as shown in Figure S15b. To reduce the effect of the noise in *iR* compensation, i_2 can be smoothed before applying eq 19. As shown in Figure S15c, smoothing by a 100-point moving average significantly helps the recovery of the corrected CV.

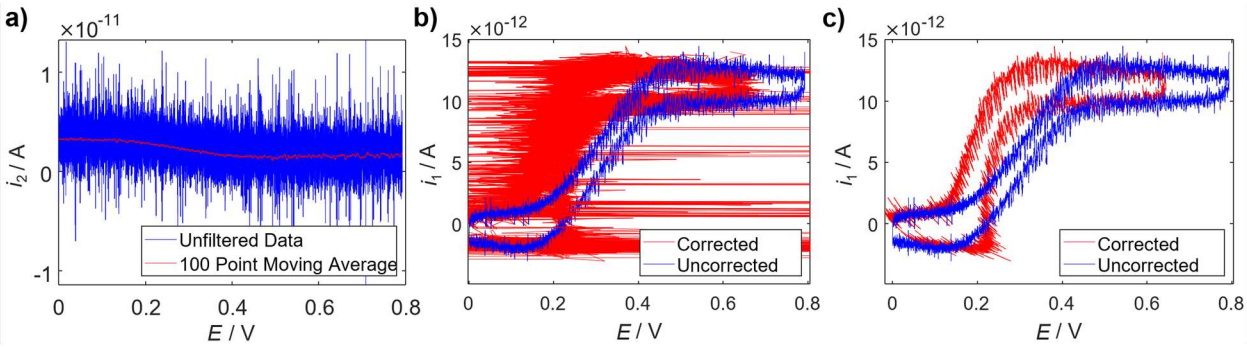

Figure S15. Effect of noise on *iR* compensation in dual-barrel SECCM a) Raw (blue), and smoothed (red) current between the barrels (i_2). b) voltammogram before (blue) and after *iR* correction (red) using raw i_2. c) voltammogram before (blue) and after *iR* correction (red) using smoothed i_2. The solution contains 20 mM Fc and 1 mM $TBAPF_6$. The substrate is Pt with bias potential V_2 = 0.1 V.

8. References

1. Kang, M.; Momotenko, D.; Page, A.; Perry, D.; Unwin, P. R. Langmuir 2016, 32 (32), 7993−8008.